JOURNAL OF MATERIALS SCIENCE 24 (1989) 23–40

Review
Acoustic microscopy of low-ductility materials

D. G. P. FATKIN, C. B. SCRUBY*, G. A. D. BRIGGS
*Department of Metallurgy and Science of Materials, Oxford University, Oxfordshire OX1 3PH, and *Materials Physics and Metallurgy Division, Harwell Laboratory, Didcot, Oxfordshire, OX11 0RA, UK*

Acoustic microscopy offers materials scientists not only high resolution, but also the ability to image sub-surface and surface features by its unique elastic contrast mechanisms. It is a particularly powerful tool for detecting discontinuities such as voids and cracks, and for characterizing interfacial boundaries between different phases. This paper describes the application of acoustic microscopy to two important classes of low-ductility material: engineering ceramics and ceramic–fibre composites. Images of a wide range of near-surface defects are presented for the six ceramics studied, including porosity and microcracks. An application to crack length determination during indentation tests is also discussed. In the composites, there were systematic variations in contrast from the fibre–matrix interface, which appeared to correlate with changes in interfacial strength. Finally, the line-focus microscope was used to demonstrate how the Rayleigh velocity and attenuation can be used to characterize the microstructure of ceramics and ceramic composites.

1. Acoustic microscopy

This paper describes the application of acoustic microscopy to the study of two important classes of low-ductility material, engineering ceramics and ceramic–fibre composites. The potential for acoustic waves as an alternative to optical waves in microscopy was identified as early as 1936 by S. Y. Sokolov [1] of the USSR, and extended in 1959 by Dunn and Fry [2] at the University of Illinois. They recognized that the lower velocity of acoustic waves allowed one, in principle, to achieve resolution comparable to the optical microscope, but at much lower frequencies. Subsequent studies of sound absorption and attenuation in materials paved the way towards the realization of a practical instrument for producing acoustic images. The breakthrough was to scan the specimen relative to a focussed acoustic beam [3].

The first scanning acoustic microscope (SAM) operated in transmission. A sapphire lens focused the acoustic waves through a coupling fluid to a point on the axis of the lens. The transmitted sound was monitored by using a similar lens to collect the scattered beam and convert it into an electrical signal. The image field was constructed point by point as the object was moved in a raster pattern through the focus of the beam. This transmission microscope operated at 160 MHz, but it was soon followed by a reflection instrument [4] operating at 600 MHz. In this instrument continuous wave (cw) electronics was used, and the specimen reflections could be distinguished from those internal to the instrument, because they were the ones which changed as the lens was scanned. Further development led to the use of pulsed (i.e. gated cw) acoustics, so that the reflections from the object could be distinguished in time from other spurious reflecting points within the system. This is now the most common method of imaging in the SAM.

Lemons and Quate [4] continued to develop the SAM, concentrating on improving the resolution of the instrument. In principle, this should be possible merely by increasing the frequency of operation of the SAM. However, acoustic waves at high frequencies are rapidly attenuated in any fluid medium (for almost all fluids attenuation increases as the square of the frequency). Therefore, to increase the resolution of the microscope, a coupling fluid was needed which did not attenuate the sound too greatly, the radius of the lens had to be decreased and the driving electronics needed to be considerably improved. In 1978, Jipson and Quate [5] achieved resolution comparable to that of the optical microscope, at an operating frequency of 3 GHz, and using warm water as the couplant. Since then, other coupling fluids have been used with varying degrees of success, including liquid helium, gallium and mercury. Resolutions of 20 nm have been obtained using liquid helium [6], significantly better than the optical microscope. The most commonly used coupling fluid is warm distilled water, in which a resolution of 0.7 μm can routinely be obtained in a standard instrument [7].

Resolution is not the only significant feature of the microscope. The most useful characteristics of the instrument for materials science fall into two distinct categories. The first is the ability to image subsurface features in materials which are opaque to other types of radiation. This is fully exploited in the transmission microscope. In the reflection instrument, which was used for this study, some of the acoustic waves from

0022–2461/89 $03.00 + .12

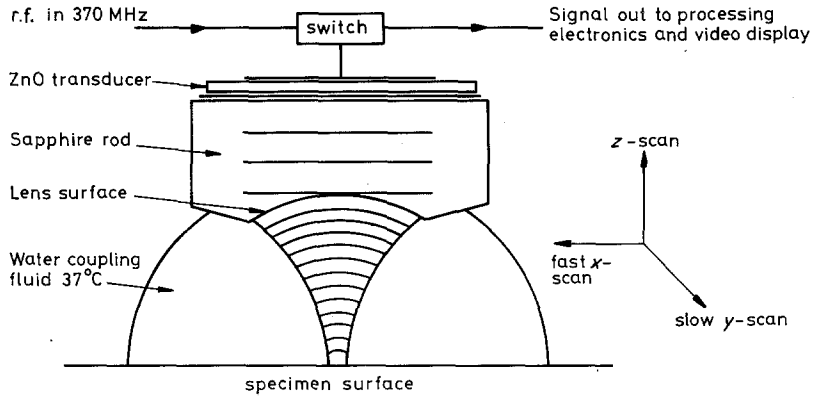

Figure 1 The acoustic lens.

the large aperture lens generate Rayleigh waves on the surface of the specimen that leak energy back into the lens system. The Rayleigh waves penetrate the specimen to a depth of approximately 1 to 2 wavelengths. Depending on the focusing conditions, the Rayleigh waves interfere with the direct reflection from the surface to give image contrast that is a function of surface and sub-surface features.

The second advantage is the fact that the acoustic image is produced by the ultrasound as it interacts with variations and discontinuities in the elastic properties of the specimen. The Rayleigh wave is especially sensitive to variations in elastic properties: near-surface cracks, grain boundaries, interfaces between phases and voids are all imaged with good contrast [8]. The interaction of these Rayleigh waves with surface and subsurface features in a material often provides information unattainable by other analytical techniques. There is also great interest in the investigation of material anisotropy, planar bonds, interfaces, cracks, grain structures and other surface and near-surface discontinuities. For a further description of the applications of the SAM see Hoppe and Bereiter-Hahn [9].

Advantages of low-ductility advanced materials, such as stiffness, high-temperature stability, hardness and wear resistance, have resulted in their development for a wide variety of applications. However, these materials are able to support little or no plastic deformation and therefore have low fracture toughness, so that the critical defect size which can be tolerated is much smaller than in most metals and alloys. There is an urgent need for a reliable method of detection and characterization of the various defects present. The contrast mechanisms in acoustic microscopy make it particularly sensitive to the type of surface and sub-surface defects which are found in these materials. This paper therefore reports the application of SAM to two major classes of low-ductility material, i.e. engineering ceramics and ceramic–fibre composites. In the single-phase ceramics, the main motivation is the detection of a range of defects, including porosity and microcracks. It will be seen, however, that SAM can also make a significant contribution to materials characterization and fracture toughness measurement by diamond indentation. In the composite materials it is the matrix–fibre interface that largely controls the mechanical strength of the material, and the acoustic microscope has, therefore, been used to study this interface.

2. Experimental techniques

2.1. The scanning acoustic microscope

The acoustic microscope used in this study operated in the reflection mode. The lens (shown schematically in Fig. 1) is made from a sapphire rod, orientated with its crystallographic *c*-axis coincident with the lens axis. One end of the rod is polished to optical flatness, while the other is spherically ground to form a concave acoustic lens. A piezoelectric transducer, consisting of a layer of zinc oxide (ZnO) sandwiched between two layers of gold, is bonded to the planar end of the sapphire rod. The front surface of the rod is coated with a layer of chalcogenide glass (As, S, Se: 40, 40, 20), one-quarter of a wavelength thick, as an anti-reflection coating between the coupling fluid (water) and the sapphire.

A block diagram of the r.f. system is shown in Fig. 2. A pulse modulated r.f. signal excites the piezoelectric transducer, which then generates an acoustic pulse which propagates the length of the sapphire rod to the lens. Some of the acoustic energy is reflected at the lens–fluid boundary, but the remaining energy in the pulse propagates into the coupling fluid in the form of a spherical wave which converges to a narrow waist at the focal plane. The specimen is positioned at the focal plane where it reflects much of this acoustic energy back through the lens into the sapphire where it is detected by the transducer. Pulsed radiation

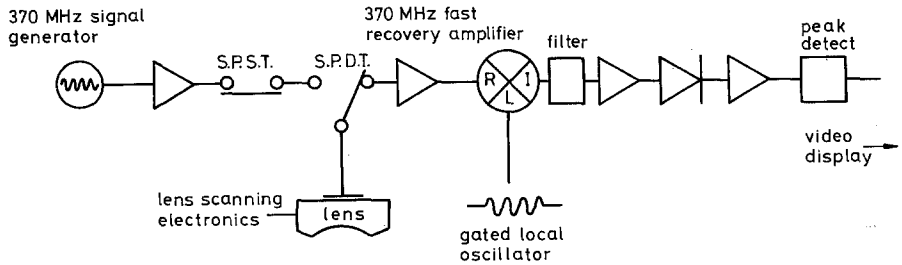

Figure 2 The Oxford scanning acoustic microscope, block diagram.

is used so that the signals of interest are separated from the lens–liquid echo and other spurious reflections. The electrical signal corresponding to the pulse reflected from the specimen is amplified and rectified by a diode detector which gives an output proportional to the square of the amplitude of the r.f. pulse. The output signal from the microscope may be displayed in two ways. The first is a line-scan on an oscilloscope (lens position = x-coordinate; signal intensity = y-coordinate). The second type of display is the conventional acoustic image, produced by feeding the signal via a framestore to a television monitor. The images are then recorded photographically. The system also permits the digital storage of experimental line-traces and $V(z)$ data in a computer.

The lens is mounted between two leaf-springs, and can be moved in fast x-scan and/or y-scan modes. An optical microscope can be inserted for direct comparison between the two types of image. The specimen is mounted on a stage with the usual facilities for translation in the x and y directions, and focusing in the z direction. The stage itself consists of a small copper heating block mounted on a platform that can be tilted using two perpendicular micrometers. The whole microscope is mounted on a massive block of cast iron, which in turn rests upon a pneumatic suspension to reduce vibration.

For satisfactory operation of the SAM it is most important to understand the effect of varying the focal conditions on the contrast in the resulting acoustic micrograph [3]. The focal plane of the lens is referred to as $z = 0$, and moving the specimen towards the lens is referred to as negative defocus (i.e. $z < 0$). The variation of the output signal with the distance between the specimen and the acoustic probe, $V(z)$, consists of a series of peaks and troughs as the lens is moved away from focus towards the specimen. Much useful information is obtained at negative defocus. Ray theory has been used to explain the $V(z)$ effect and therefore the change in contrast with defocus [10, 11]. In this approach there are two waves contributing to the image: the first is incident at the Rayleigh angle, and the second incident normally. The interference between these two waves as a function of defocus explain the oscillations in $V(z)$, and thus the change in contrast.

Because a complete reversal of contrast can be expected for very small changes in z (as little as 5 μm in some materials, even less at higher frequencies), a deviation in flatness or a tilt of the specimen can produce a series of dark and bright fringes across the image. Even a small misorientation can lead to a progressive change in the contrast which might lead to the image being misinterpreted. It is thus essential that the specimen is flat and level. The specimen also needs to be polished (1 μm diamond paste) and clean. This ensures that the contrast achieved is not due to surface topography, but to the interaction of Rayleigh waves with the microstructure of the specimen.

2.2. The line-focus-beam acoustic microscope (LFBM)

The variation of the output of a piezoelectric transducer, V, with the distance between the acoustic probe and the specimen, z, is known as the $V(z)$ effect. The shapes of $V(z)$ curves are unique and characteristic of solid materials. If a relationship between the elastic properties of these materials and their corresponding $V(z)$ curves exists, then one has the basis for a method of material characterization.

There are several distinct types of acoustic wave involved in the propagation of sound in a solid. In addition to the more familar bulk longitudinal and shear waves, acoustic energy can also propagate along the surface of an elastic solid as Rayleigh waves. The Rayleigh wave is bound to the surface, and its amplitude within the solid decays exponentially away from the surface. If the solid is in contact with a fluid such as water, energy is progressively radiated away from the Rayleigh wave into the fluid during propagation, and the wave is then referred to as a "leaky" Rayleigh wave. Determining the propagation characteristics (i.e. velocity and attenuation) of these Rayleigh waves is helpful in characterizing the material.

In 1979, Weglein [12] reported that the periodicity of the peaks and troughs in the $V(z)$ curves measured experimentally were closely related to the corresponding Rayleigh wave velocities. Further investigation confirmed that this phenomenon was due to interference between the leaky Rayleigh wave and the specularly reflected wave, and a mathematical model became available [13]. As a result it is possible to deduce the Rayleigh wave velocity and attenuation from experimental $V(z)$ data for a given material.

The line-focus microscope was developed as a tool for materials characterization based on the principles described above [14]. A cylindrical lens is used to produce a line-focus beam, rather than a point-focus beam (as produced by the spherical lens in conventional SAM). The reason for this is that the point-focus system excites leaky Rayleigh waves in all directions simultaneously: therefore, measured acoustic properties are averaged over all angles in the surface of the material. The line-focus arrangement is more satisfactory for studying materials with appreciable anisotropy. The acoustic line-focus beam is achieved by a sapphire lens with a cylindrical concave surface. The lens was made to give optimum performance at 225 MHz, but it was found that it would operate satisfactorily over the range 120 to 300 MHz. A schematic diagram of the lens is shown in Fig. 3. Many of the features present are identical to those of the spherical lens used in the SAM, because the principle of operation is the same.

The electronic system is almost identical to that used for the SAM. Computers are used to control the system and perform the $V(z)$ analysis. This acoustic lens is automatically translated in a direction perpendicular to the sample. Measurements can be made as a function of orientation by rotating the specimen stage. As with the point-focus SAM it is necessary to ensure extremely good alignment between the specimen and the transducer. Temperature stability is also most important. Distilled water is used as the couplant, and the temperature of the water and the acoustic frequency of operation are

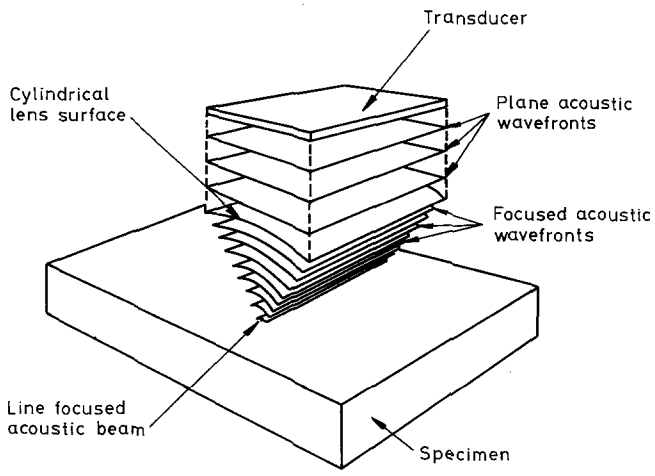

Figure 3 The Oxford line-focus-beam acoustic microscope, schematic diagram.

both fed into the computer while measurements are in progress.

The main steps in the analysis of the $V(z)$ curves are as follows (for a full description see Kushibiki and Chubachi [14]). The key to the analysis is to represent the transducer output $V(z)$ by the equation: $V(z) = V_I(z) + V_L(z)$. $V(z)$ represents the experimental measurement of the transducer output. $V_I(z)$ represents the contribution of the Rayleigh wave to the transducer output. $V_L(z)$ is the output for a material upon which no Rayleigh wave is excited, and is usually obtained by measuring the experimental $V(z)$ curve for polytetrafluoroethylene (PTFE). If the $V_I(z)$ curve can be extracted from the experimental data, then the velocity and attenuation of the leaky Rayleigh waves may be calculated from mathematical expressions which have been derived using ray theory. The computer programme incorporates moving average filtering techniques and fast Fourier transforms.

There are some substantial limitations to the use of the line-focus-beam acoustic microscope. The use of water coupling allows accurate measurement of velocities between approximately 2000 and 11000 m sec^{-1}, and normalized attenuations from about 1×10^{-3} to 1×10^{-1}. A different lens and fluid would be required for measurements outside these ranges. In particular, the $V(z)$ analysis of highly attenuative materials cannot be carried out with the present system because the Rayleigh wave is attenuated before it generates sufficient interference oscillations for any measurements to be made from the data. In materials of lower attenuation, velocities are measured with an accuracy approaching 0.02%, and attenuations with an accuracy of a few per cent. This accuracy makes the line-focus instrument extremely useful for quantitative materials characterization.

3. Engineering ceramics

Ceramics are being increasingly used for engineering applications in hostile environments such as the high temperatures within an internal combustion engine. The performance of these high-strength low-ductility materials depends critically upon the size of any defects that might be present. Acoustic microscopy has attracted much interest recently as a potential non-destructive evaluation (NDE) technique for detecting and sizing surface and sub-surface defects. We have used the SAM and LFBM to investigate possible applications to engineering ceramics, including the characterization of microstructure, especially porosity and defects. We also investigate the use of the SAM to measure crack length (from which fracture toughness can be calculated) during Vickers indentation tests. An additional important potential application is the characterization of machining damage, and it is planned to study this in the future.

3.1. Characterization of microstructure by SAM

Samples of six engineering ceramics were examined in the SAM: (a) Vitox alumina, (b) sialon, (c) silicon carbide, (d) reaction-bonded silicon nitride (RBSN), (e) HZ44 zirconia, (f) TZ3Y zirconia. Acoustic micrographs of typical areas of all six specimens under the same imaging conditions are shown in Fig. 4. The most striking difference in the microstructures is the variation in the porosity. As expected, the most porous material (d) is the RBSN. The alumina and sialon specimens are relatively featureless, the alumina (a) having very low porosity.

It is interesting to compare the two zirconia specimens, HZ44 and TZ3Y. Zirconia exists in three distinct crystal phases: above 2300° C it is cubic, between 1150 and 2300° C it is tetragonal, and below 1150° C it occurs in a monoclinic phase. The stability of these phases can be altered by alloying. The transformation from tetragonal to monoclinic zirconia occurs by a martensitic mechanism which is accompanied by a volume expansion of about 4%. This expansion causes a degree of transformation toughening, in addition to microcrack toughening if, after transformation, the expansion is constrained by internal stresses. Under these mechanisms it is possible to manufacture very strong and tough zirconia-based ceramics. The two samples being considered in this work have small additions of yttria (Y_2O_3), which stabilizes the tetragonal phase. The network of microcracks is visible in HZ44, Fig. 4e, and to a lesser degree in TZ3Y (Fig. 4f). The difference between the images of these specimens is consistent with differences in manufacture. The TZ3Y material contained a higher percentage of yttria, and was pressed from a more finely divided powder.

All the specimens gave the most contrast in the

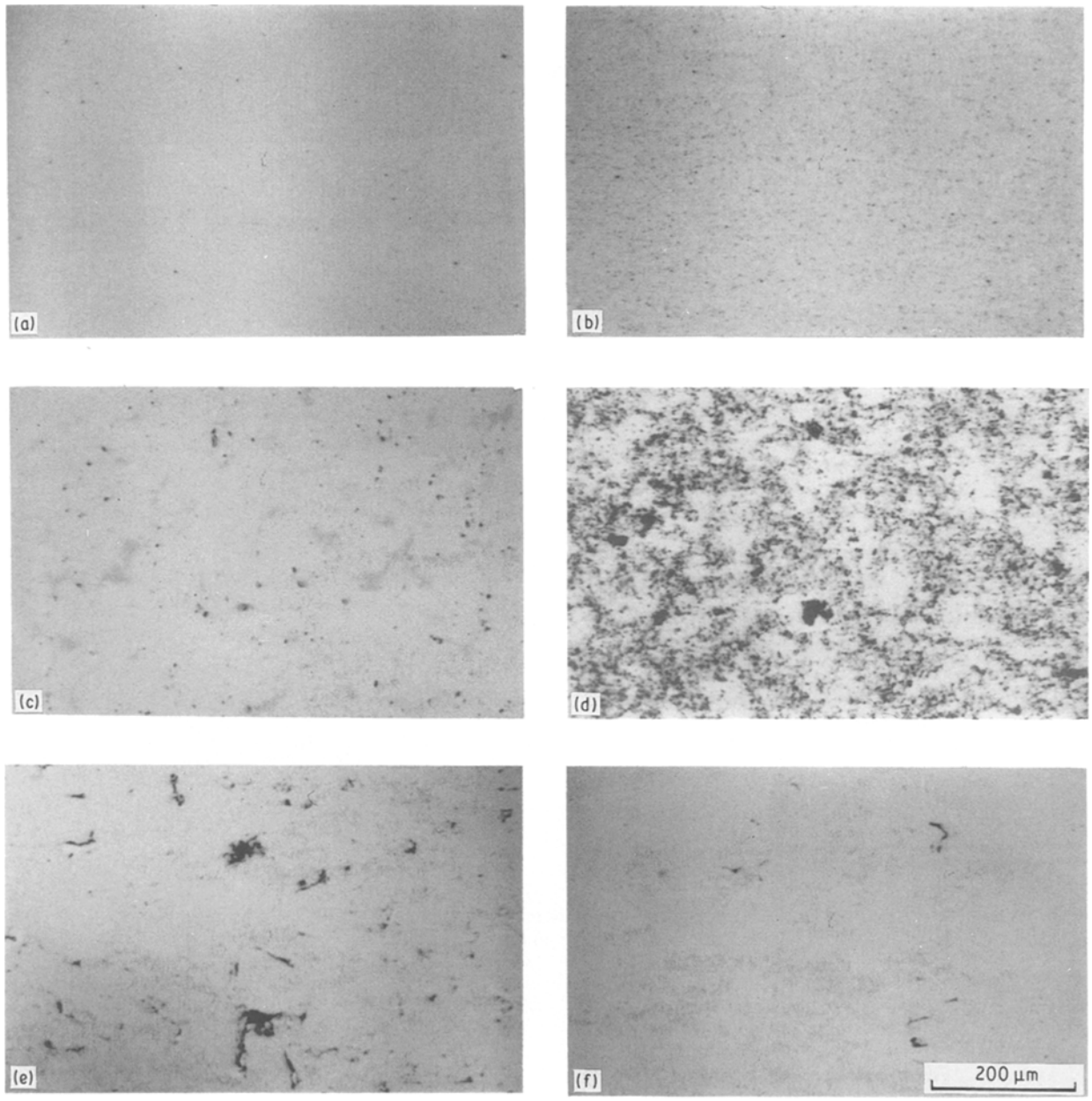

Figure 4 Acoustic images taken at focus comparing the microstructures of (a) Vitox alumina, (b) silicon carbide, (c) sialon, (d) reaction-bonded silicon nitride (RBSN), (e) TZ3Y zirconia and (f) HZ44 zirconia.

region of negative defocus (i.e. with the lens moved towards the sample), and one example of the effect of defocus is given in Fig. 5. This shows a microcrack in the TZ3Y specimen, taken (a) at focus, and then (b) at 10 μm defocus. Note the characteristic fringes (b), which arise at least partly through Rayleigh wave interference effects. Defocus also enhances the contrast in Fig. 6, which shows a microcrack in HZ44. The fringes are less marked in Fig. 6c than in Fig. 5b even though it is at the same defocus. This may be because the defects in Fig. 6 are not perpendicular to the surface. Stronger fringes occur at larger values of defocus (20 to 30 μm) but the image may then be more difficult to interpret. The light areas that appear around some of the defects in Fig. 6 at negative defocus are believed to indicate damage extending out from the surface-breaking defects below the surface. Similar contrast is observed from the lateral cracks accompanying indentation, and is discussed in more detail below.

The ability of the SAM to image subsurface features (generally invisible to other forms of radiation) is illustrated in Fig. 7, which shows a typical area of the SiC specimen. At focus (Fig. 7a) the microstructure appears as a pattern of dark pores against a background of much lighter patches, which are believed to correspond to pores beneath the surface. As the negative defocus is increased to $-10\,\mu$m (Fig. 7c), thereby altering the interference conditions, the subsurface pores are imaged with comparable contrast to the surface pores in (a). Under these conditions, yet more pores, which are situated deeper below the surface, begin to be visible.

3.2. Characterization of microstructure by LFBM

The LFBM was used to investigate the same specimens as those studied in the SAM. The long-axes of the specimens were aligned parallel to the direction of propagation of the Rayleigh waves, which was

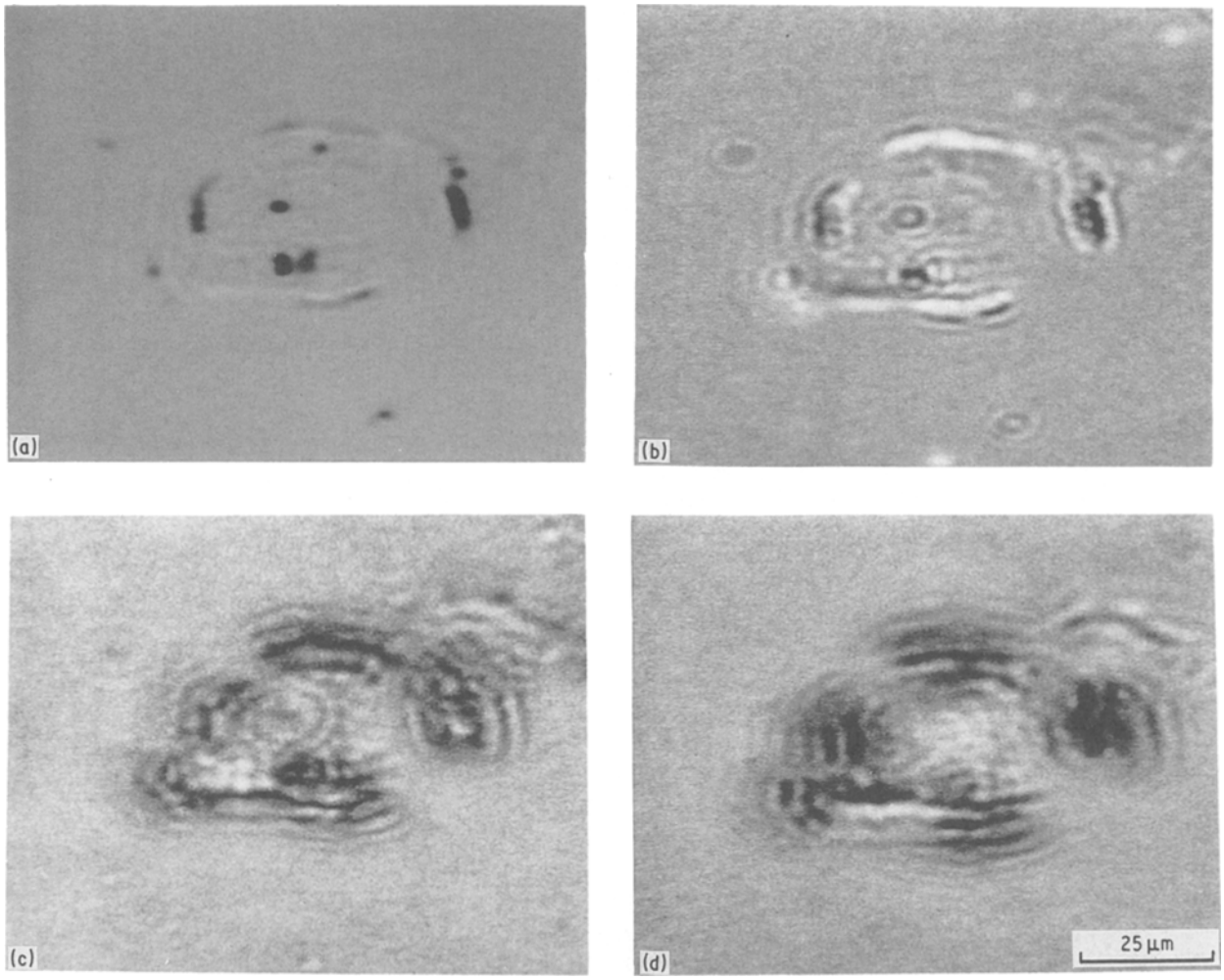

Figure 5 Microcracking in TZ3Y zirconia, illustrating the associated interference fringes. Images were taken at (a) focus, (b) $z = -10\,\mu m$, (c) $z = -20\,\mu m$ and (d) $z = -30\,\mu m$. Note the effect of defocus on these fringes.

denoted as 0°. Experimental $V(z)$ curves were then recorded at 15° intervals between 0 and 90° rotating the lens anti-clockwise. All measurements were made at 228 MHz and repeated several times to check reproducibility. The experimental $V(z)$ curves for each specimen at 0° are shown in Fig. 8. These results illustrate the wide range of acoustic (and hence elastic) properties exhibited by this group of engineering ceramics. The Rayleigh wave velocity is calculated from the period (z) of the damped oscillations in $V(z)$, and given by the equation

$$z = v_W/2f(1 - \cos\theta_R)$$

where $\sin\theta_R = v_W/v_R$, v_W is the longitudinal velocity in water, v_R is the Rayleigh wave velocity, and f is acoustic frequency. A large period, as for instance in silicon carbide, Fig. 8c, therefore indicates a high velocity. A small period (e.g. TZ3Y zirconia, (Fig. 8f) indicates a relatively low velocity. The attenuation is calculated from the exponential rate of decay of the oscillation in $V(z)$. Thus the attenuation is relatively low in alumina (a) and high in RBSN (d). Attenuation is caused by several factors: the leaking of energy into the coupling fluid (distilled water in this case), bulk acoustic absorption, and scattering by surface toughness, grains, pores and boundaries. In the measurement of both these properties, any significant changes as the specimen is rotated about the z-direction would correspond to anisotropy within the material of the kind discussed.

The Rayleigh wave velocity and attenuation were computed for each angle, and the results given in Table I. These data indicate that all the specimens are relatively isotropic except for RBSN, for which the velocity and attenuation both vary considerably. This could be due to anisotropy, though it is difficult to be certain because of the considerable scatter in the results. RBSN usually has a porosity of 15 to 20%, (cf. Fig. 4d). As a consequence, the Rayleigh wave velocity and attenuation must be extremely variable locally. Furthermore, the attenuation also exceeds the experimental limit for accuracy. By reducing the frequency, the LFB microscope could possibly be used to measure the degree of porosity within a material such as RBSN. Because ultrasonic attenuation increases rapidly with frequency in highly scattering materials, there would be considerable benefit in working at lower frequencies.

The difference between the data for the two zirconia specimens is encouraging. The greater degree of microcracking observed in the HZ44 specimen compared with TZ3Y (Fig. 4e, f) imply that the Rayleigh wave attenuation should be higher and the velocity lower, and that there should be more scatter in the data for the former. Table I confirms that the attenuation in HZ44 is almost double that in TZ3Y zirconia,

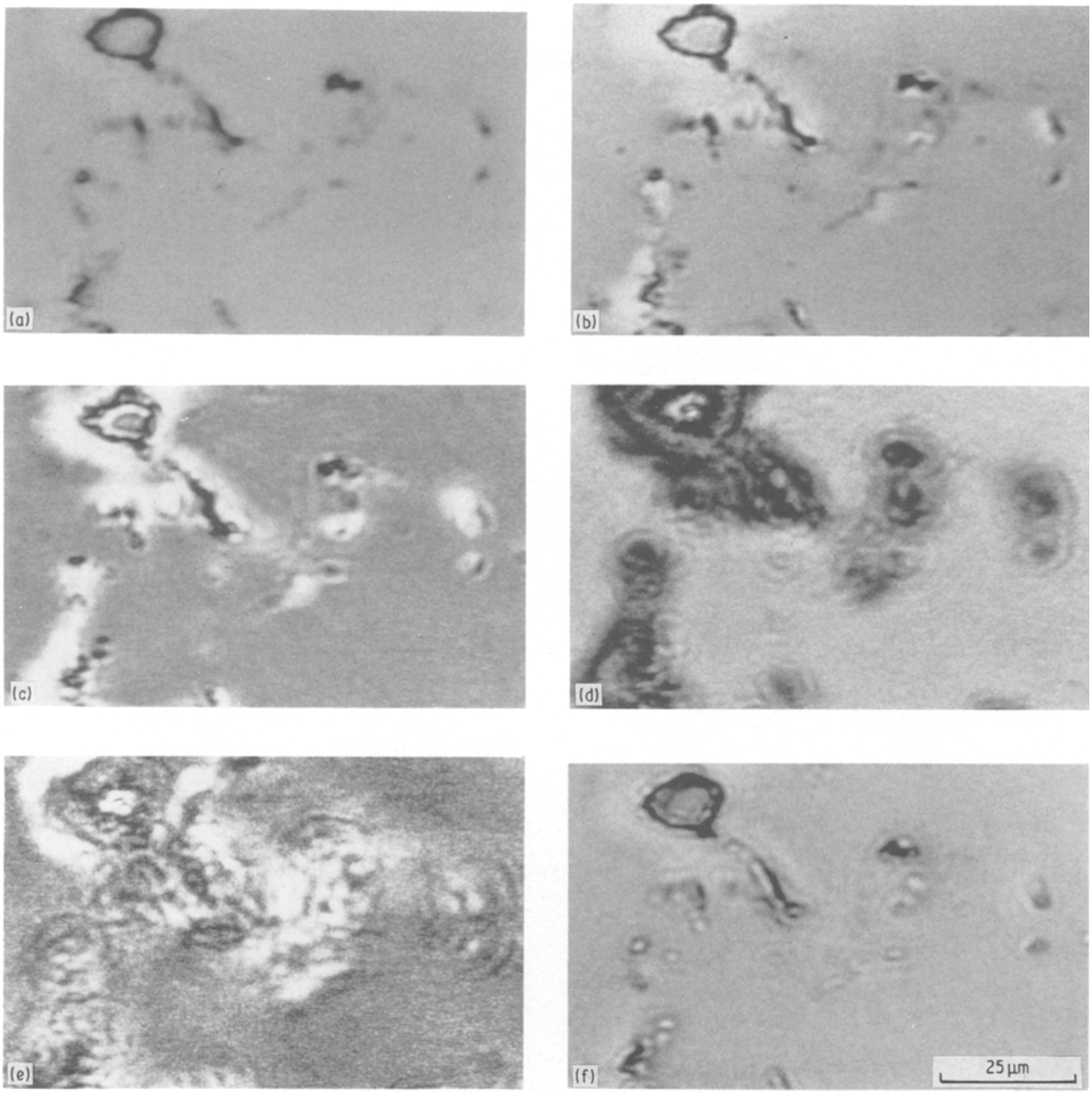

Figure 6 Microcracking in HZ44 zirconia at (a) focus, (b) $z = -5\,\mu m$, (c) $z = -10\,\mu m$, (d) $z = -20\,\mu m$, (e) $z = -30\,\mu m$ and (f) $z = +10\,\mu m$. Note the contrast reversal as the defocus is increased (a consequence of the $V(z)$ effect).

and that the average velocity is 1.6% lower. In both the sialon and alumina there is little change in the Rayleigh wave propagation with direction, and less attenuation than the other materials. This is consistent with the low concentration of defects observed in the SAM (Fig. 4). It is noted that the values of Rayleigh wave velocity and attenuation will vary from sample to sample depending on their preparation and history.

3.3. Crack characterization in Vickers indentation tests by SAM

The indentation test is now well established as a standard indicator of material "hardness" and fracture toughness. The most common form of indentor is the "sharp" indentor (i.e. cone or pyramid), where elastic/plastic stress fields govern crack development. The cracks which are induced can be divided into two

TABLE I Rayleigh wave velocity and attenuation of engineering ceramics as measured using the LFBM. The angle is 0° when the long axis of the specimen is parallel to the direction of propagation of the Rayleigh waves

Angle (deg)	Velocity ($m\,sec^{-1}$)						Attenuation (normalized $\times 10^{-1}$)					
	Alumina	Sialon	Sic	RBSN	HZ44	TZ3Y	Alumina	Sialon	SiC	RBSN	HZ44	TZ3Y
0	5841.4	5548.7	6784.7	4628.4	3340.3	3396.3	0.1037	0.1115	0.3390	0.7370	0.2347	0.1350
15	5844.1	5532.4	6712.3	5808.4	3345.6	3398.0	0.1058	0.1274	0.2849	2.0050	0.2135	0.1348
30	5833.9	5542.3	6748.4	5018.8	3340.7	3397.9	0.1179	0.1114	0.2516	0.8830	0.2208	0.1296
45	5844.0	5561.4	6747.8	4695.7	3352.1	3397.7	0.1123	0.1096	0.2220	0.6780	0.2189	0.1330
60	5834.1	5540.3	6751.3	4688.1	3345.5	3394.5	0.1084	0.1182	0.2649	0.4490	0.2045	0.1286
75	5834.3	5540.0	6752.9	4749.1	3330.2	3394.6	0.1116	0.1190	0.3114	0.5980	0.2418	0.1266
90	5825.1	5546.6	6763.9	5024.1	3337.1	3395.8	0.1144	0.1154	0.1959	1.0040	0.2456	0.1256

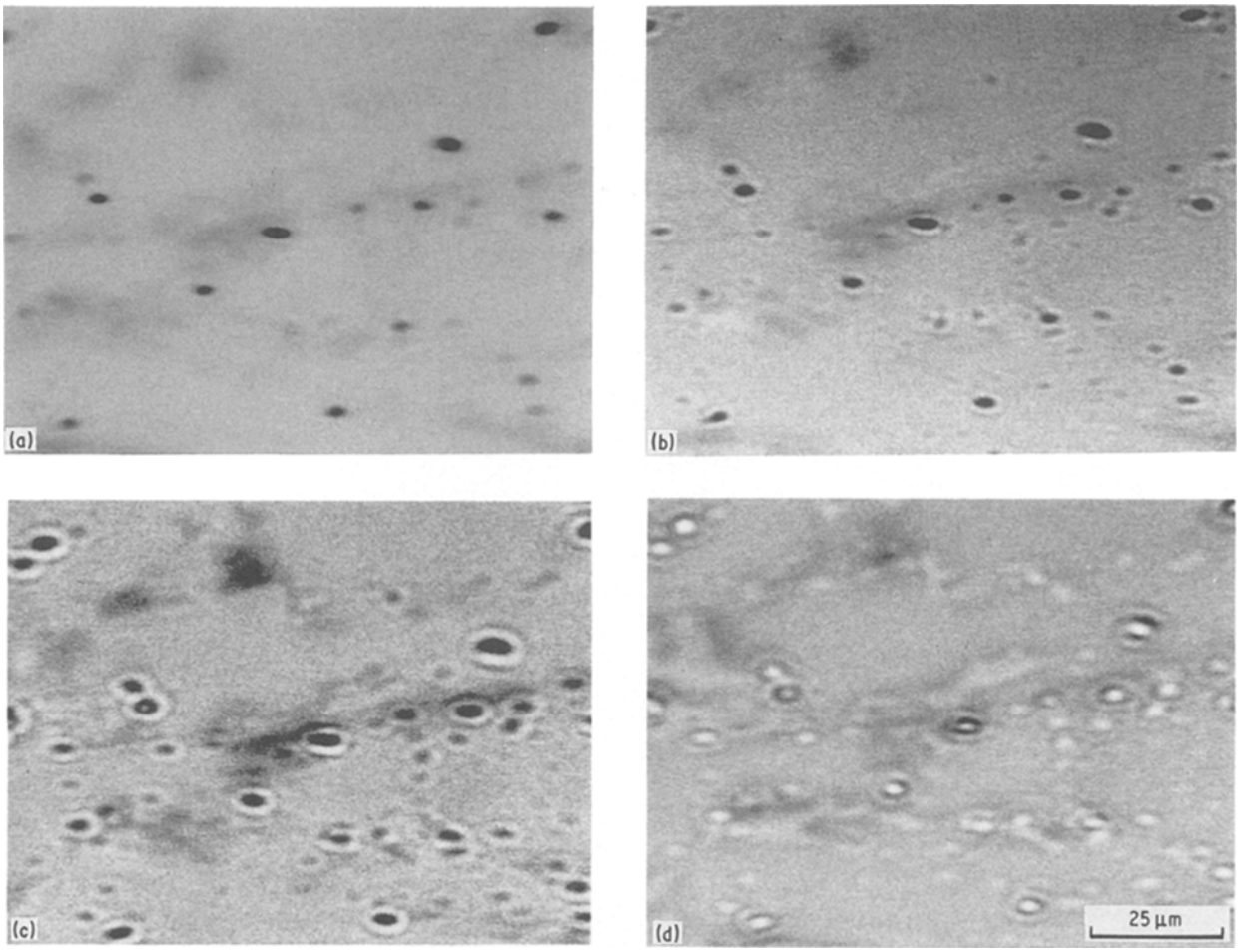

Figure 7 Porosity in silicon carbide, taken at (a) focus, (b) $z = -5\,\mu m$, (c) $z = -10\,\mu m$ and (d) $z = +10\,\mu m$.

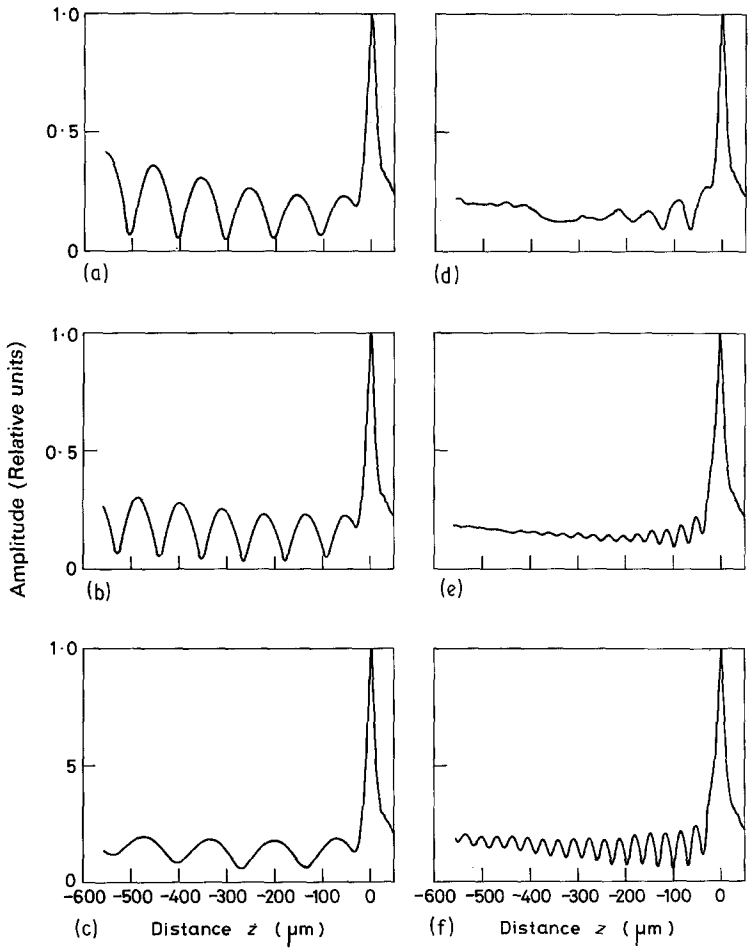

Figure 8 Experimental $V(z)$ curves for (a) Vitox alumina, (b) sialon, (c) silicon carbide, (d) RBSN, (e) HZ44 zirconia and (f) TZ3Y zirconia.

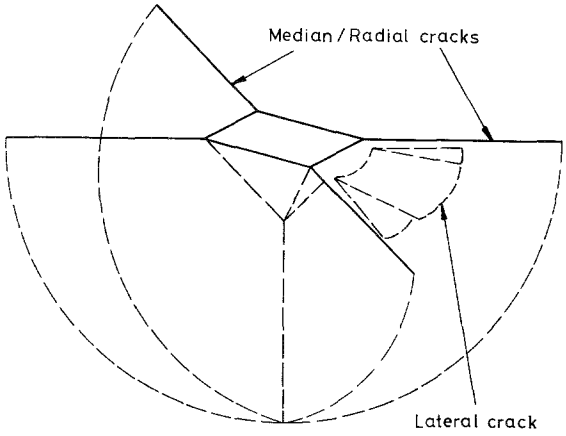

Figure 9 Schematic diagram of the median/radial crack system resulting from a Vickers indentation.

distinct systems: the "median" ("radial") crack system, and the "lateral" crack system. The former refers to those cracks which form on symmetry (median) planes containing the load axis, and the latter concerns those cracks which form laterally on planes approximately parallel to the specimen surface (Fig. 9).

Investigations into the fracture mechanisms of the crack systems described above were reported by Lawn and Wilshaw [15]. A relationship was determined [16], between the fracture toughness, K_c, and the length of the cracks, c, which emanate from the corners of the impression produced by a Vickers pyramid indentor. In their analysis the final crack configuration continues to evolve as the indentor is removed from the surface, due to the residual stress field. In this calculation of fracture toughness using the equation defined above, it is crucial to obtain an accurate measurement of c, the length of the radial cracks. The end of these cracks is often in doubt in optical or scanning electron micrographs, especially when residual stress causes the crack to close at the surface. The SAM was therefore proposed as a possible alternative technique, because the Rayleigh waves should interact extremely strongly with the radial cracks. It was also hoped that the subsurface lateral cracks would be visible at either positive or negative defocus.

A Vickers indentor was used to introduce cracks into partially stabilized zirconia (PSZ), REFEL silicon carbide (SiC), hot-pressed silicon nitride (HPSN), and reaction-bonded silicon nitride (RBSN). The loads applied varied between 1 and 75 N, and they produced a wide variety of crack patterns. In the zirconia (PSZ), the radial cracks were straight, and the surrounding microstructure did not mask the profile of the indent (Fig. 10). At focus (Fig. 10a) the contrast from the radial cracks is weak and it is difficult to see where they terminate. However, at $-35\,\mu$m defocus the cracks are made visible by characteristic fringes. These fringes are imaged at values of defocus where the interference conditions between the Rayleigh wave and the specularly reflected wave are optimized. Another indent in the same specimen is shown at a higher magnification in Fig. 11. The radial cracks end abruptly, and by taking the average length of the cracks and the fringes alongside them, a more accurate value for the fracture toughness may be calculated.

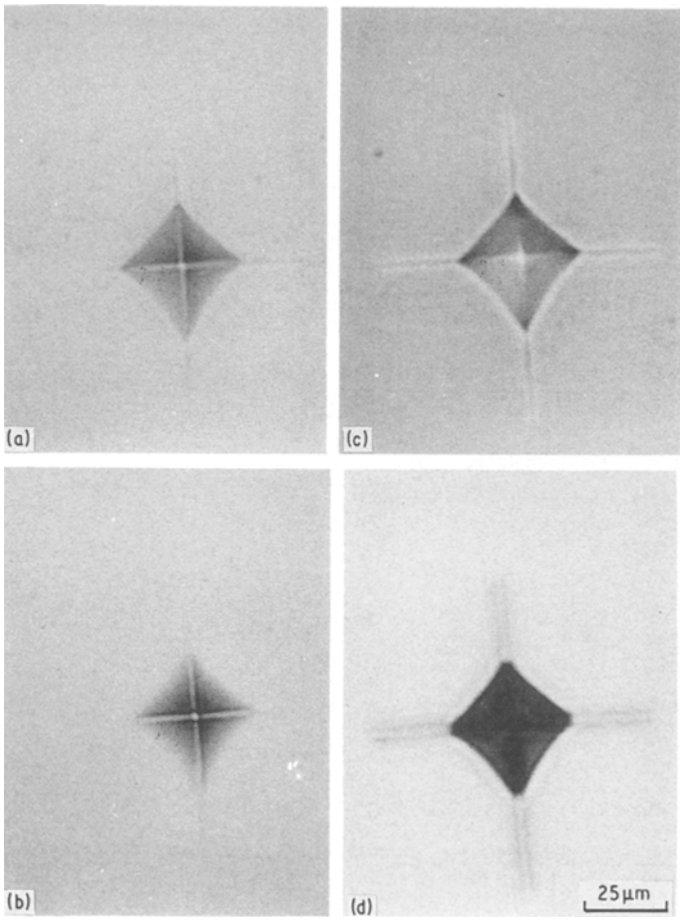

Figure 10 Acoustic micrographs of a 5 kg Vickers indentation in partially stabilized zirconia (PSZ) at (a) focus, (b) $z = -15\,\mu$m, (c) $z = -25\,\mu$m and (d) $z = -35\,\mu$m. Fringes associated with the radial cracks are observed at large defocus.

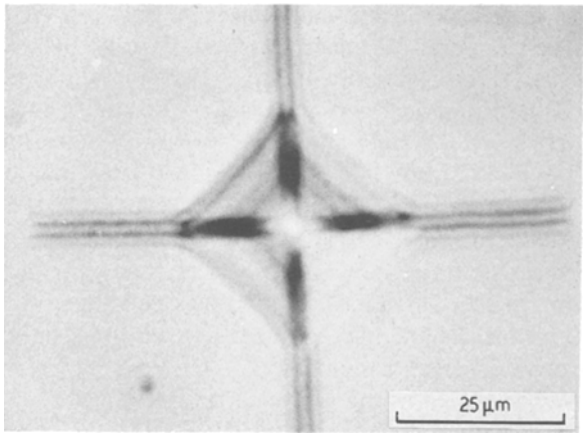

Figure 11 7.5 kg indentation in PSZ taken at $z = -30\,\mu m$, showing strong interference fringes around the radial cracks.

Yamanaka *et al.* [17] have also shown the good contrast that the SAM gives for radial cracks in hot-pressed silicon nitride.

Yamanaka *et al.* [18] predicted that a subsurface lateral crack produced by an indentor should be observed as a region which is considerably brighter than crack-free material, when the lens is moved slightly towards the surface (i.e. negative defocus). The images of the indentations of Fig. 12 in PSZ confirm that this is the case. At $-20\,\mu m$ defocus (Fig. 12b), only the radial cracks are visible, but as negative defocus is increased to $-55\,\mu m$ (Fig. 12c), what is believed to be lateral cracking begins to appear as dark contrast around each indentation. Some caution is necessary in interpreting these images, because the rise in the surface around each indentation caused by the flow of material can also give rise to contrast variations. Topography is not, however, thought to be the origin in these images because the contrast only occurs at values of defocus in excess of $50\,\mu m$. A further point of interpretation is that the damage in this material is more likely to take the form of a distribution of microcracks than a single lateral crack. At $-65\,\mu m$ (Fig. 12d) the full extent of the sub-surface damage can be observed as regions of bright contrast in the image. Lateral cracks are very difficult to image and size by other means, so that the ability to image both crack systems simultaneously in the SAM should prove most valuable to the study of ceramics.

These results illustrate the potential of acoustic microscopy for crack measurement. PSZ is, however, a relatively easy material for Vickers indentation measurements by conventional microscopy. The images in SEM or optical microscopy become more difficult to interpret when harder materials, or ones with more complicated microstructures are tested. These materials do not produce the straight cracks of PSZ. Fig. 13 shows SAM images in the three other ceramics that were subjected to indentation tests. In RBSN (Fig. 13a) the profile of the indentation is not

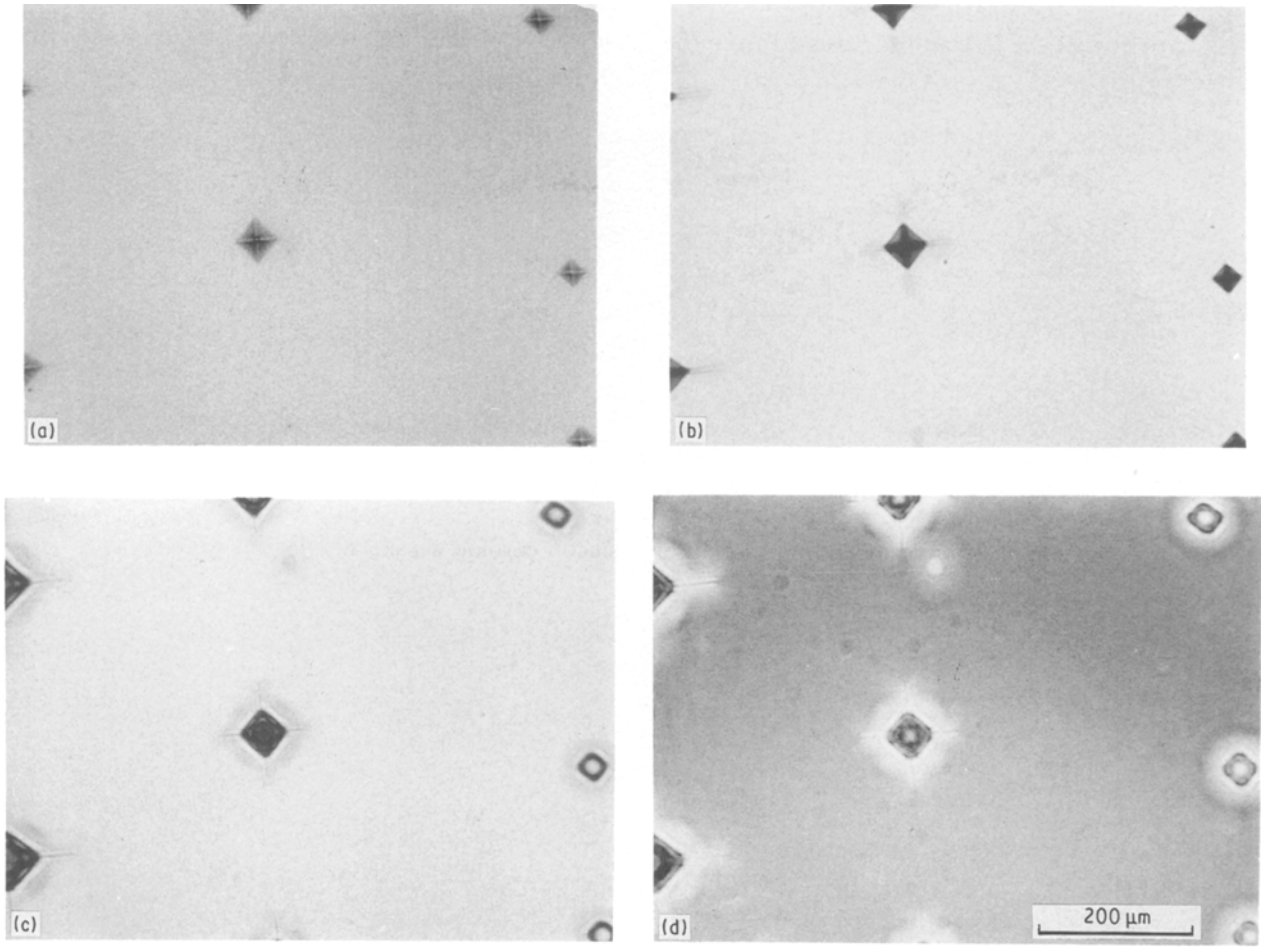

Figure 12 Indentations in PSZ at (a) focus, (b) $z = -20\,\mu m$, (c) $z = -55\,\mu m$ and (d) $z = -65\,\mu m$. The dark circles around the indentations in (c) may represent subsurface damage in the form of lateral cracking. The contrast of this area reverses in (d) as a consequence of the $V(z)$ effect. Indentations at left, centre and right of the micrographs at respectively 7.5, 5.0, 2.5 kg.

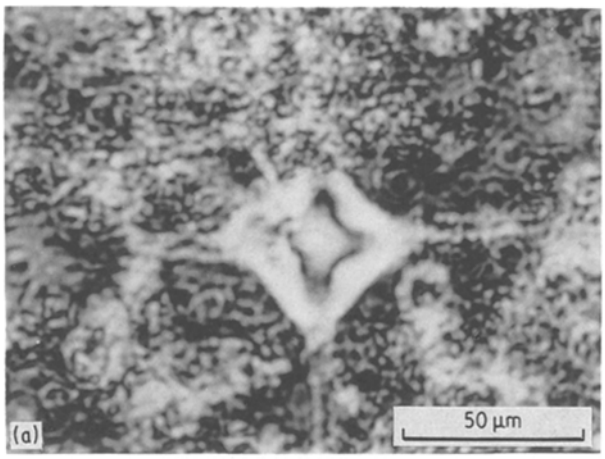

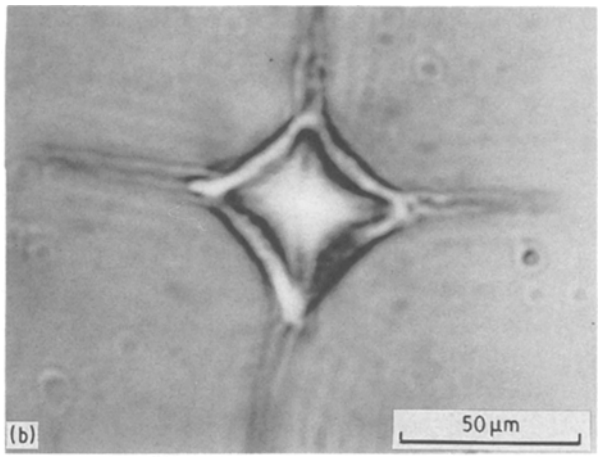

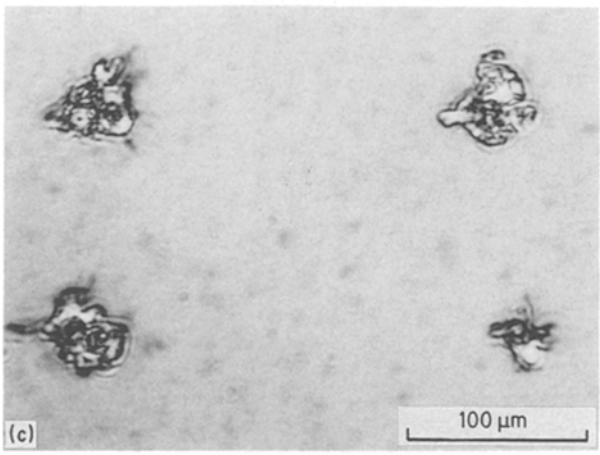

Figure 13 Indentations in (a) reaction-bonded silicon nitride taken at $z = -10\,\mu m$ (2.5 kg), (b) hot-pressed silicon nitride (HPSN) at $-10\,\mu m$ (2.5 kg), (c) in silicon carbide at $-15\,\mu m$ (1 kg). At defocus fringes become visible around the radial cracks.

symmetrical and there is considerable background contrast. This is because of the high porosity and hardness of RBSN, and it is an example of a situation when the crack is difficult to image in SEM and optical microscopy. However, using the SAM at $-10\,\mu m$ defocus the contrast is enhanced sufficiently to measure the extent of the cracks.

HPSN is much less porous than its reaction-bonded counterpart, and the radial cracks (Fig. 13b) can be imaged almost as well, therefore, as in PSZ. In this region the cracks are not disturbed by pores. In other regions of the material where the pore density was slightly higher it was observed that radial cracks were sometimes arrested by pores.

Silicon carbide proved to be a difficult material in which to produce an acceptable indentation because of its inherently high hardness. However, at $-15\,\mu m$ defocus (Fig. 13c) the SAM provides some useful information on the extent of subsurface damage, and there is a suggestion of radial cracking extending from at least two of the indentations shown.

In addition to direct materials evaluation, Vickers indentation tests also have important applications in, for instance, erosion and wear studies. The results presented above indicate the potential for SAM as a technique for quantifying the extent of damage in all these areas.

4. Ceramic–fibre composites

The motivation for using acoustic microscopy to study engineering composites lies in its sensitivity to interfaces where there is an elastic mismatch, either at or below the surface. Investigations in the past have used optical microscopy, SEM, and dye penetrant techniques, but none of these is able to obtain sub-surface information non-destructively in opaque materials. In addition to imaging sub-surface features, there are further advantages of acoustic microscopy for the study of engineering composites. These arise because the variation of contrast with defocus (the $V(z)$ effect) is strongly dependent upon changes in elastic properties. There is a large difference in acoustic impedance between the fibres and the matrix in most composites. Thus acoustic waves in general, and the Rayleigh wave in particular, undergo strong reflections from these interfaces, and give good contrast in most composite materials. Any other surface and subsurface cracks and discontinuities will also be detected. The LFBM can, furthermore, be used to detect the distribution and orientation of fibres within a matrix. For the use of both these instruments, specimen preparation is straightforward, a $1\,\mu m$ diamond polish sufficing.

The investigation was conducted on three different composite materials. These were silicon carbide fibre-reinforced aluminium (Alsic), silicon carbide fibre-reinforced pyrex (Pysic), and alumina reinforced with silicon carbide whiskers.

4.1. SAM images of composite materials

The first specimen to be studied was the metal–matrix composite, Alsic. This specimen had been in a three-point bend test, and the damaged area could therefore be studied closely. Interest was initially directed towards imaging subsurface fibres. As Fig. 14 shows, although this sample had no special surface preparation, it is still suitable for study on the SAM. The technique enables individual fibres to be imaged with excellent contrast. Fig. 15 shows a different area at higher magnification. Again there is excellent contrast at focus (Fig. 15a). As the lens is moved towards the specimen different sections of fibre A in the damaged region beome visible below the surface. Note also

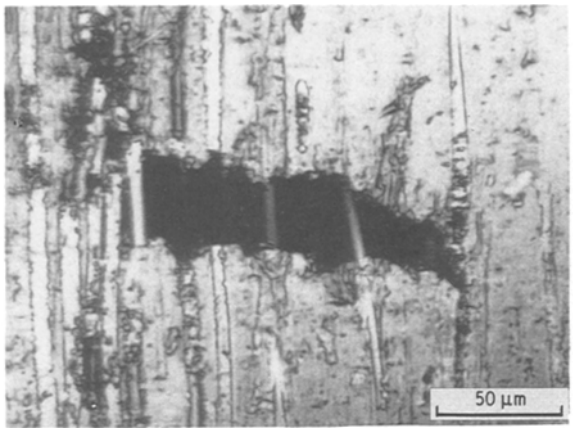

Figure 14 Acoustic image of a damaged area of the Alsic specimen.

the ripples within fibre B, and the contrast at the fibre/matrix interface. Fig. 15b shows the image at a defocus of $-10\,\mu m$.

The Pysic specimen was polished to give a $1\,\mu m$ finish on a flat, clean surface. Some surface damage was observed which was probably induced during the polishing process. An example of a damaged area is shown in Fig. 16 at varying defocus, which reveals several interesting features.

(i) The weak fringes that can be seen running parallel to the fibre in Fig. 16a and d, e.g. just to left of the central fibres. These were less clearly resolved in the Alsic specimen). The fringes are believed to be due to reflections of the Rayleigh wave at the fibre/matrix interface discussed earlier. They are observed to be perturbed where the interface is perturbed, so that they could possibly indicate the quality of the fibre/matrix bond, and whether any disbonding has occurred.

(ii) The contrast from the fibre/matrix interface when the fibres pass beneath the surface of the specimen. Note how the contrast along fibre A varies with the focusing conditions.

(iii) The dark outline along the edge of the fibres. This could either be the first fringe of the type discussed above, or a result of the polishing to expose parts of the fibre to the surface. This effect is most marked at smaller values of defocus (Fig. 16b). Here, however, the dark outline is also observed along fibre A where it is buried beneath the surface so that is cannot be entirely due to polishing.

(iv) The structure observed between and perpendicular to the central fibres at greater values of defocus (especially in Fig. 16c). The origin is not clear.

(v) The fringes visible within the fibres at positive defocus as in Fig. 16d. These could indicate some matrix overlay, especially if the fibres are partially disbonded from the matrix.

Fig. 17 shows a nearby area in the Pysic sample. It confirms the strong contrast from the fibre/matrix interface both at and below the surface, and shows the fringes within the fibres particularly well. Finally, Fig. 18 shows a region at higher magnification. This has been chosen because it shows more clearly the Yamanaka fringes (Y) to the left of the main fibres in the image, the contrast from fibre/matrix interfaces when they are buried beneath the surface, and the

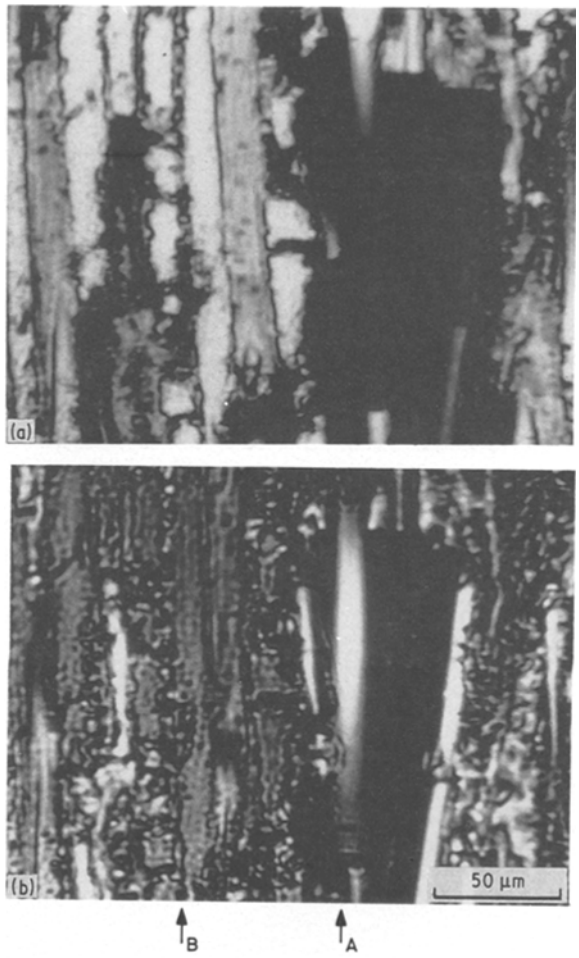

Figure 15 Another damaged area in the Alsic specimen, taken at (a) focus, (b) $z = -10\,\mu m$.

fringes within the fibres at positive defocus (Fig. 17b). These micrographs show that much information is available in the region of the fibre/matrix interface. For closer study it was decided that single-fibre specimens were more appropriate.

4.2. Single-fibre specimens

Four single-fibres Pysic specimens were separately fabricated to produce different quality bonds at the fibre/matrix interface. In each specimen the fibre was submerged just beneath the surface and was fractured in a flexure test. Both halves were retained and studied carefully on the SAM. The aim of the investigation was to correlate the images obtained on the SAM with the quality of the interfacial bond. It was also hoped that the results for each sample could be correlated with fibre pull-out measured after the fracture of specimens prepared in a similar manner. The preparation details are given in Table II.

Fig. 19 shows the first specimen, A, at various values of defocus. The fibre in this specimen was air desized at 800° C and underwent no further treatment.

TABLE II Preparation details

Specimen identity	Fibre preparation	Results of flexure tests
A	Air desized at 800° C	Short pull-out
B	Graphite coated (bad wetting)	Long pull-out
C	Acetone-washed prior to embedding	Long pull-out
D	High-temperature fabrication	Short pull-out

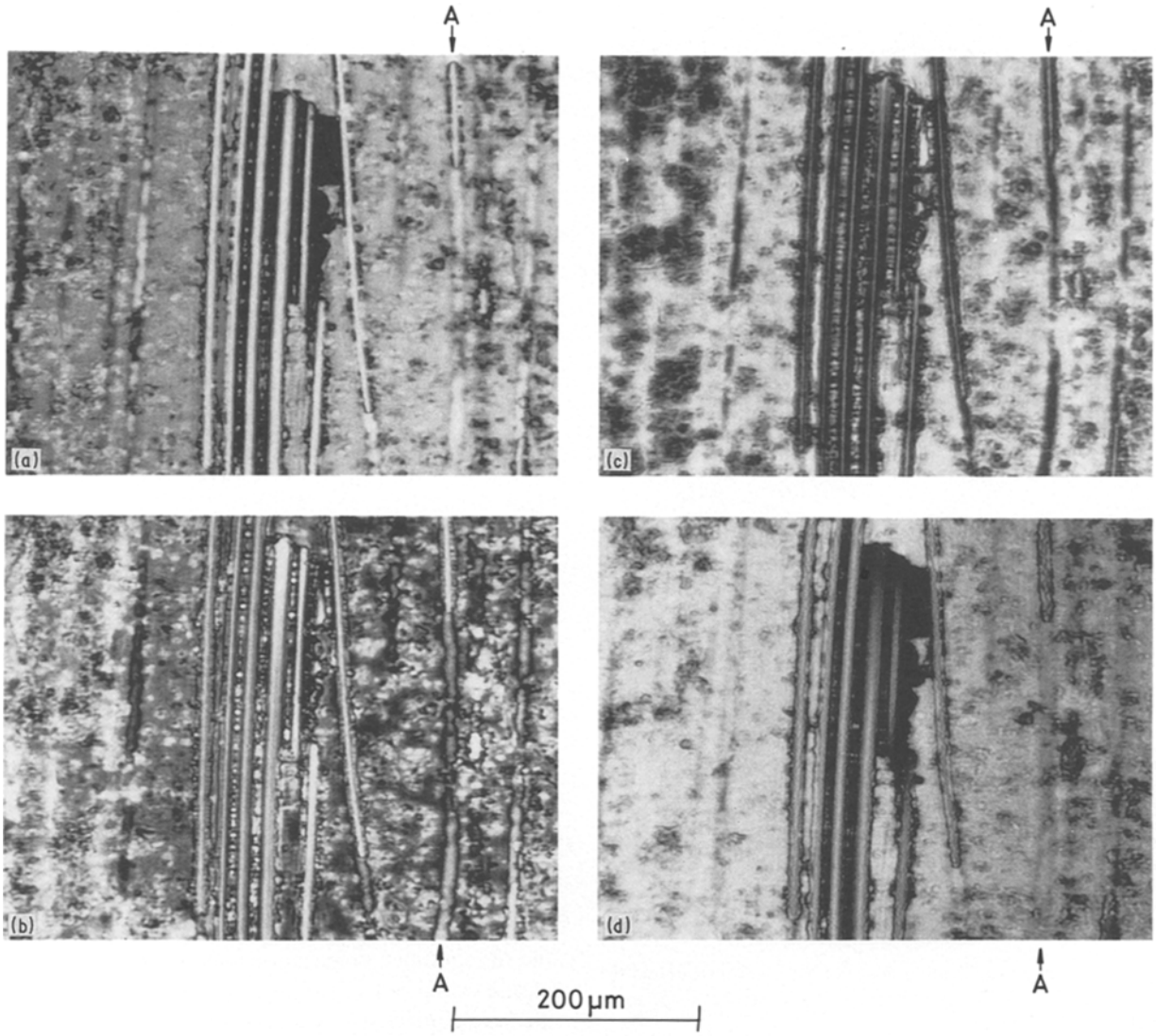

Figure 16 Damaged area of Pysic specimen at (a) focus, (b) $z = -5\,\mu m$, (c) $z = -10\,\mu m$ and (d) $z = +5\,\mu m$. Fringes are observed parallel to fibres (a), and within fibres (d). Note also strong outline around fibres, and structure between central fibres (especially in (c)).

The fibre was expected to be quite well bonded to the matrix, and comparable to the Pysic material tested above. As in Fig. 16 there is an outline around the fibre when uncovered and when buried. The intensity of this outline for the buried portion of the fibre in (Fig. 19b) does not greatly vary, and could therefore indicate a successful bond. Fig. 20 shows two perpendicular fibres in the same specimen. These fibres are at different depths in the matrix, and at defocus this difference can be detected quite easily by the change in contrast between the two (Fig. 20b). It is noted that for those areas along the fibre running vertically in (Fig. 20a) which have not been uncovered by polishing, there is a corresponding bright area in (Fig. 20b). These bright areas could indicate the extent of the fibre/matrix bond, so that any discontinuity in intensity might represent a partially disbonded area.

In the second specimen, B, the fibre was badly

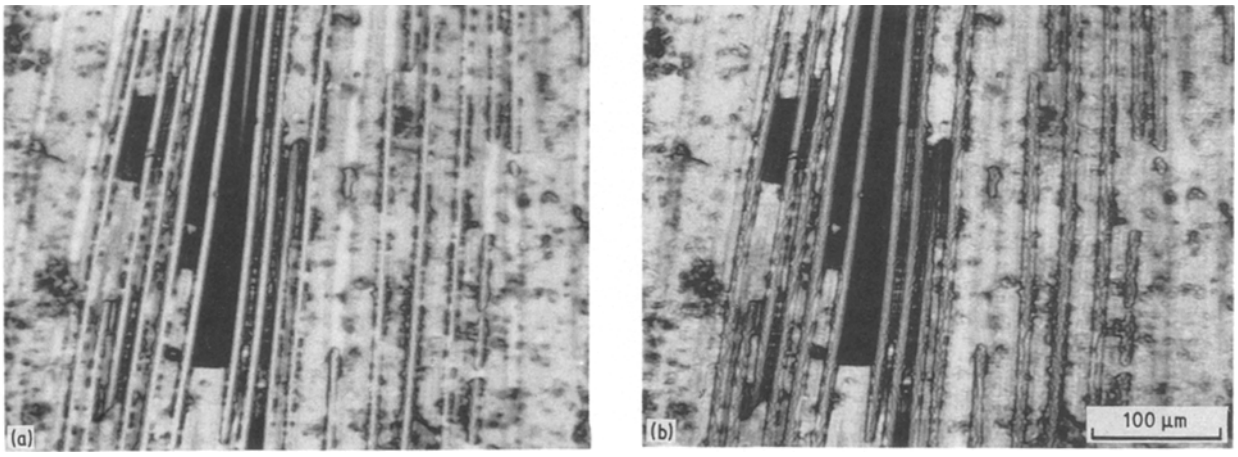

Figure 17 Nearby area of Pysic at (a) focus and (b) $z = +5\,\mu m$. Characteristic fringes associated with the fibres are again observed.

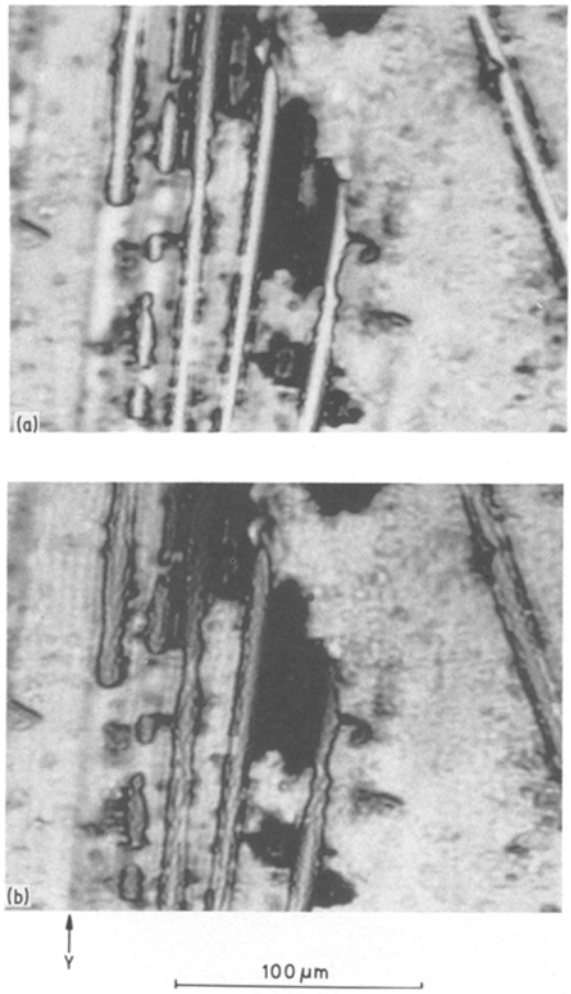

Figure 18 Higher magnification image of Pysic at (a) focus and (b) $z = +5\,\mu m$. Notice that fibre contrast is still significant for areas which are below surface.

wetted by coating with a graphite layer to produce what was expected to be a fibre/matrix bond of low strength. The fibre was quite deep in the pyrex matrix, and at times difficult to view. An example of the acoustic micrographs obtained of this fibre is given in Fig. 21a. The outline along the fibre is much less pronounced, and at this defocus it appears slightly brighter than the matrix. This might be a result of the greater depth of this fibre compared with A. Alternatively, the fibre/matrix interface might be qualitatively different, which would be consistent with the difference in fibre pull-out at fracture.

In the preparation of the next specimen, C, the fibre was acetone-washed before it was embedded in the matrix. The image of this fibre (Fig. 21b) is comparable with the graphite-coated specimen. The fibre is well below the surface again. Fig. 21b has been processed using image enhancement to improve what would otherwise have been very low contrast.

The final single-fibre specimen, D, was prepared by a high-temperature fabrication method which was expected to produce a strong fibre/matrix bond but an inferior energy of fracture to specimen A. Fig. 22 shows a typical area in this material, in which the matrix has "crazed". At focus there is strong contrast along the fibre/matrix interface. A defocus of $-15\,\mu m$ (Fig. 22b) gives high contrast for the fibre (to be compared with Fig. 19b) in addition to imaging the crack boundaries due to the crazing.

Thus specimens A and D were similar in giving high-contrast outlines for the fibre/matrix interfaces, whereas specimens B and C both gave weak contrast. These observations can be compared with the results of the fibre pull-out tests. The materials corresponding to specimens B and C behaved in a similar manner in the flexure test, giving rather large pull-out lengths. The materials corresponding to the other two specimens (A and D) also had similar pull-out lengths, but these were considerably shorter than B and C, thereby indicating greater bond strength. However, to perform these comparisons reliably and eliminate any depth-dependent contrast effects in the SAM, the fibres should all be at the same depth beneath the surface, and the specimen preparation and polishing should not expose the fibre to the surface. It is not yet clear why the lower interfacial strength of specimens B and C should give less contrast in the SAM than the stronger interfaces in A and D, rather than the converse. We note, however, that one contributory factor could be the thermoelastic stresses that result from thermal expansion coefficient differences between pyrex glass and silicon carbide. The stronger interfaces would inhibit stress relief on cooling, leaving a residual strain field around each fibre.

A further specimen was fabricated using the same method as for specimen A, and a section normal to the fibre axis prepared. This was then studied on the SAM, and some of the images obtained are presented in Fig. 23. At focus in the SAM (Fig. 23a) there

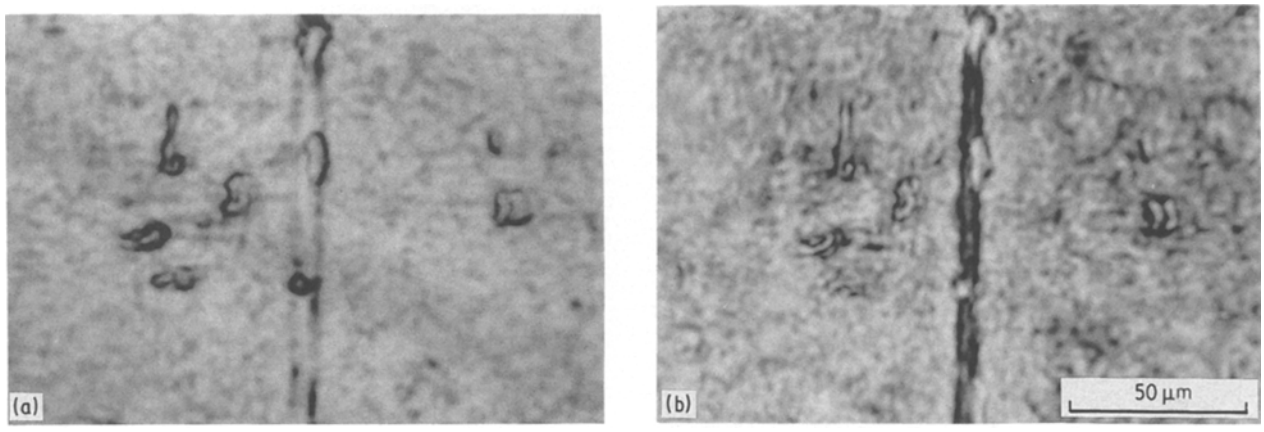

Figure 19 Acoustic images of single fibre Pysic specimen A (optimized fibre/matrix bond) taken at (a) focus, (b) $z = -8\,\mu m$.

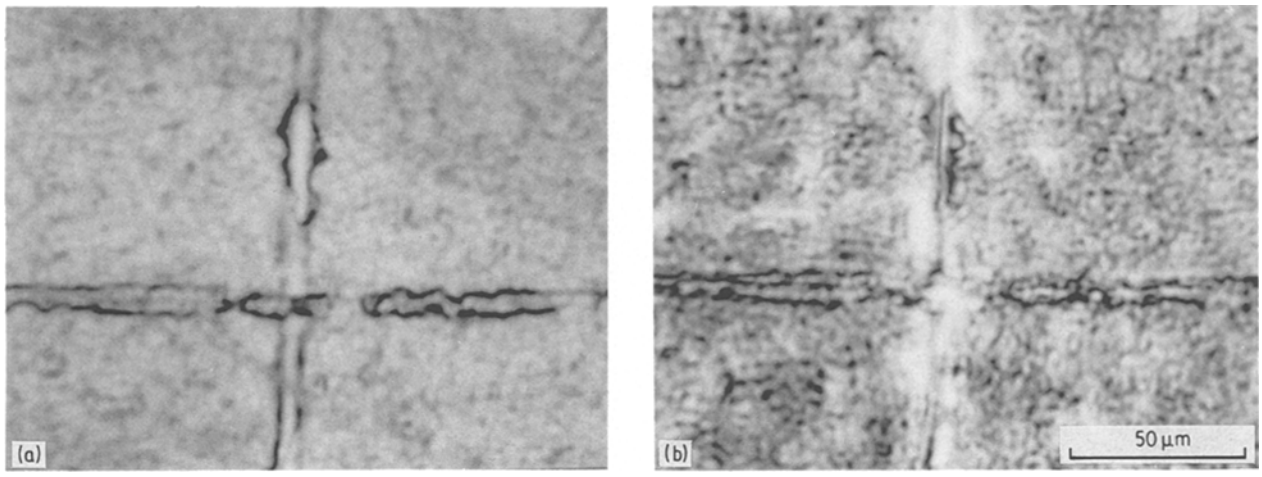

Figure 20 Two perpendicular fibres in specimen A at (a) $z = -8\,\mu m$, (b) $z = -14\,\mu m$. Notice change in contrast between the two fibres in (b), showing they are at different depths in the matrix.

are two regions on the interface with stronger contrast. Furthermore at $-15\,\mu m$ defocus (Fig. 23b) characteristic fringes appear, whose contrast changes in the same two regions. These areas are opposite each other, and it is possible that they may correspond to some variation in bonding resulting from imperfect fabrication. It would clearly be profitable to study oblique sections of a range of single-fibre specimens, using progressively degraded fibre/matrix bonds. The work outlined in this section is most encouraging, and further investigations could lead to a complete characterization of the fibre/matrix interface.

4.3. Characterization of microstructure by LFBM

In this section the LFBM is investigated as a method for determining the distribution, orientations and adhesion of fibres in reinforced materials. The study was carried out first using the Pysic specimen from which Fig. 16 was obtained. The experimental procedure followed is outlined in Section 2, to give the $V(z)$ curve of Fig. 24. From this the Rayleigh wave velocity and attenuation data (Table III) were obtained, measurements being made only at 0, 45 and 90°. Compared with, for instance, Fig. 8, Fig. 24 is a poor $V(z)$ curve, because of high attenuation in the composite. Under such conditions, there could be significant errors in the values of velocity and attenuation deduced, especially in the latter. We note that Rayleigh wave velocity is comparable with silicon carbide (see Table I). There was a difference in the results between 0 and 90°, which may be due to the presence of the fibres. At 0° the Rayleigh waves are propagating in a direction parallel with the fibres, while at 90° they are perpendicular. At 0° the Rayleigh wave velocity is predicted to be higher, and this is indeed the case. A more comprehensive set of measurements would enable this material to be characterized more fully.

Measurements were also made on two specimens which were, respectively, pure alumina, and alumina reinforced with silicon carbide whiskers (approximate diameter $0.75\,\mu m$, length $10\,\mu m$). As expected, the fibres could not be resolved in the SAM at 370 MHz, and only a weak modulation in intensity was observed, probably corresponding to local variations in fibre orientation and density. In the SEM image of the fracture surface shown in Fig. 25 there appears to be some fibre orientation in the micrograph shown, although the fibres are intended to be orientated randomly. This preferred orientation may well be a local effect.

The LFBM was used to measure the angular dependence of the Rayleigh velocity and attenuation in both specimens. Table IV presents these results for the pure alumina specimen, compared with the results obtained earlier for the Vitox alumina specimen. In each case

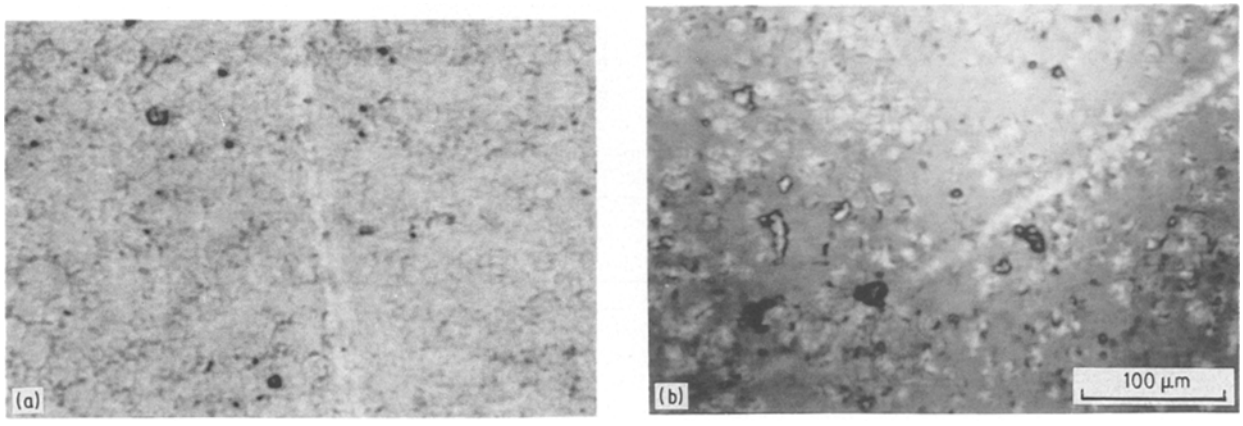

Figure 21 (a) Specimen B (graphite-coated fibre) at focus. (b) Specimen C (acetone-washed fibre) showing the fibre submerging into the matrix at $z = -4\,\mu m$.

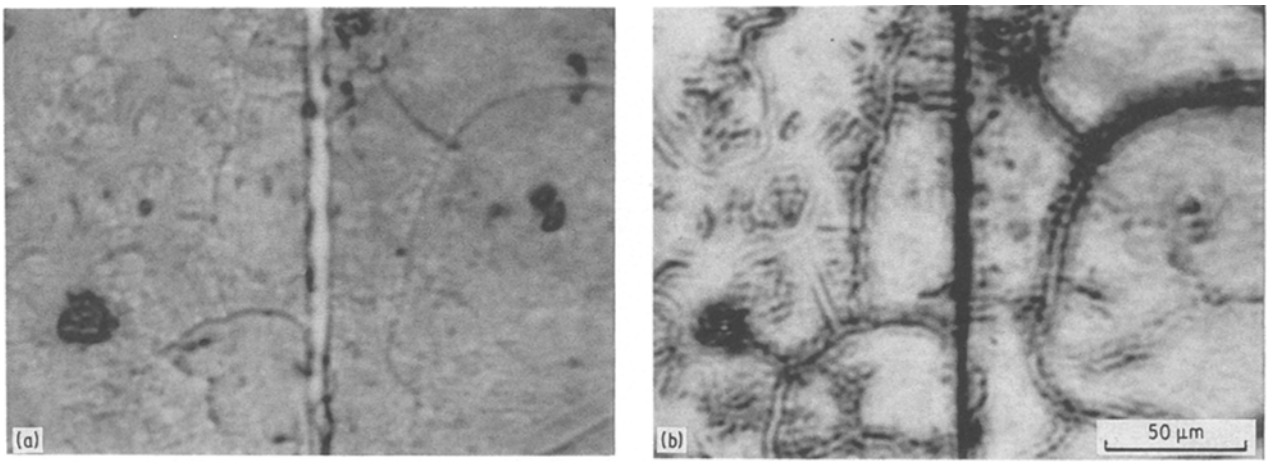

Figure 22 Single-fibre specimen D (high-temperature fabrication) taken at (a) focus and (b) $z = -15\,\mu m$.

the velocity and attenuation were deduced from the data in 15° increments of propagation direction. Both materials are almost isotropic, and with similar elastic properties. In Table V, the results obtained at two positions on the whisker-reinforced sample, A and B (which were seen to have differing degrees of fibre alignment in the optical microscope), are presented.

Table VI summarizes mean values for velocity and attenuation in each specimen. The attenuation is clearly higher in the samples containing the SiC fibres than in pure alumina. This is presumably a consequence of the increased scattering of acoustic energy at the fibre/matrix interface. The velocity measurements in the SiC fibre-reinforced specimen are particularly interesting; they may be broken down into two separate effects of fibre alignment and possible bonding effects. The angular dependence exhibited in the data for the reinforced specimen (Table V) indicates that there is some degree of preferred alignment at A and B. The data for the more parallel area (A) would be expected to show a greater angular variation, and Table V shows that this is indeed the case for attenuation.

TABLE III Rayleigh wave velocity and attenuation measurements obtained for Pysic using the LFBM. 0° when the Rayleigh waves propagate parallel to the long axis of the specimen, with which the fibres are also aligned

Angle (deg)	Velocity ($m\,sec^{-1}$)	Attenuation ($\times 10^{-1}$)
0	6764.8	0.2720
45	6758.8	0.2695
90	6740.5	0.2754

It has been proposed that the mean velocity is related to the degree of fibre bonding (for example see Datta *et al.* [19]. Some measurements to test this hypothesis have been made by David Kupperman (unpublished work), in which he compared shear wave velocities measured at 20 MHz with those predicted theoretically for both pure and whisker-reinforced alumina. The Voigt and Reuss averaging schemes predicted upper and lower limits within which the experimental results should have fallen (Table VII). In fact, the Argonne values measured for the composite were approximately 1% too low. Kupperman suggested bond degradation as the explanation for this. Estimates (Table VII) of shear wave velocities were made using the Rayleigh wave velocity measurements obtained from the same Argonne sample on the LFBM at 228 MHz. These values deviated by about 3% from theoretical expectations in the case of the composite material, and from the 20 MHz value therefore by about 1%. The data for the pure ceramic only differed by 0.1%.

If the hypothesis is correct, the present data suggest that the effect of fibre bonding on ultrasonic velocity increases with frequency, which could have significant practical consequences. However, the results must be interpreted very carefully. There are some topographical and geometrical features on the samples which may influence the Rayleigh wave velocities. These features would become more pronounced as the wavelength shortens. The data, nevertheless, show that it is worth undertaking a more comprehensive study of fibre/matrix interfacial strength using ultrasonic measurements over a wide frequency range.

TABLE IV A comparison between the Rayleigh wave velocity and attenuation measurements made on the LFBM for Vitox alumina and Argonne alumina. 0° when the Rayleigh waves propagate parallel to the long axis of the specimen

Angle (deg)	Velocity ($m\,sec^{-1}$)		Attenuation ($\times 10^{-1}$)	
	Vitox	Argonne	Vitox	Argonne
0	5841.4	5841.5	0.1037	0.1236
15	5844.1	5840.8	0.1058	0.1182
30	5833.9	5838.7	0.1179	0.1108
45	5844.0	5838.6	0.1123	0.1101
60	5834.1	5836.9	0.1084	0.1131
75	5834.3	5838.8	0.1116	0.1181
90	5825.1	5827.0	0.1144	0.1145

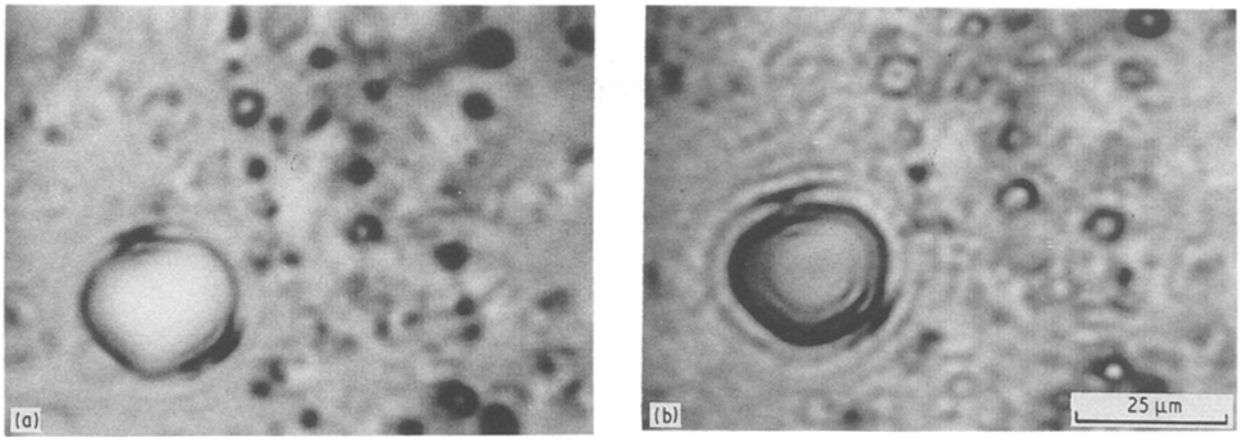

Figure 23 Acoustic micrographs of perpendicular section of single-fibre specimen with an optimized fibre/matrix bond, at (a) focus and (b) $z = -15\,\mu m$.

5. Conclusions

It is concluded that acoustic microscopy can provide information for the study of materials which is difficult to obtain non-destructively by other techniques. The results especially demonstrate the versatility of acoustic microscopy for the examination of low ductility materials. There are three major ways in which acoustic microscopy has demonstrated its strengths as a materials tool.

1. By imaging sub-surface microstructural features in the materials, such as buried pores, lateral cracks, and sub-surface fibres in the composites. These features cannot readily be imaged otherwise.

2. By imaging boundaries and interfaces where there is an elastic mis-match, giving rise to strong contrast. Some of these features (such as tight cracks) give much inferior contrast by other methods.

3. By detecting (in the LFBM) very small variations in elastic properties as a function of position or orientation on the specimen due, for instance, to preferred fibre orientation in composite.

The importance of Rayleigh waves in the generation of contrast in the acoustic micrographs presented in this work cannot be overemphasized. The images in the SAM tend to be dominated by the interaction of these waves with changes in the elastic properties of the materials. Rayleigh waves also provide the quantitative information in the LFBM which enables material properties to be characterized.

In the pure ceramics the characterization of porosity and other defects could prove to be a useful application of the SAM. It is also recommended that machining damage be studied because of its practical importance. The authors also believe that the results from indentation tests are so encouraging that SAM should be further developed as a crack length (and hence fracture toughness) measurement tool. The LFBM has potential as a relatively rapid method for characterizing the degree of surface and sub-surface porosity in these materials.

Some of the most exciting applications could, however, be to the composite materials. The contrast from the matrix/fibre interface is so strong (even for buried fibres) that information about the material is obtained extremely easily. The apparent correlation that was found between interfacial contrast and bond strength is particularly encouraging, because this is at present virtually impossible to measure nondestructively. The authors plan a comprehensive and systematic study of the fibre/matrix interface using the SAM. This study will be broadened to include measurements by LFBM to quantify the apparent frequency dependent effects due to the interfaces.

Acknowledgements

We are deeply grateful to Dr Kushibiki of Sendai University, Japan, for the provision of both acoustic lenses and for the LFB system, and to Dr Weaver of this Department, and Dr Smith and Mr Martin of Harwell Laboratory for development of the scanning acoustic microscope control system. We also wish to thank Dr A. Briggs, Dr D. Dawson and Mr R. Piller (Materials Development Division, Harwell

TABLE V A comparison between the Rayleigh wave velocity and attenuation measurements made on the LFBM for an area with more parallel whiskers (A) and an area with less parallel whiskers (B) in the alumina composite. 0° when the Rayleigh waves propagate parallel to the long axis of the specimen

Angle (deg)	Velocity ($m\,sec^{-1}$)		Attenuation ($\times 10^{-1}$)	
	A	B	A	B
0	5870.9	5853.6	0.1183	0.1519
15	5847.5	5850.2	0.1617	0.1498
30	5842.9	5842.6	0.1372	0.1350
45	5861.6	5837.7	0.1495	0.1509
60	5839.6	5838.8	0.1505	0.1338
75	5858.3	5832.6	0.1152	0.1426
90	5818.6	5809.5	0.1710	0.1502

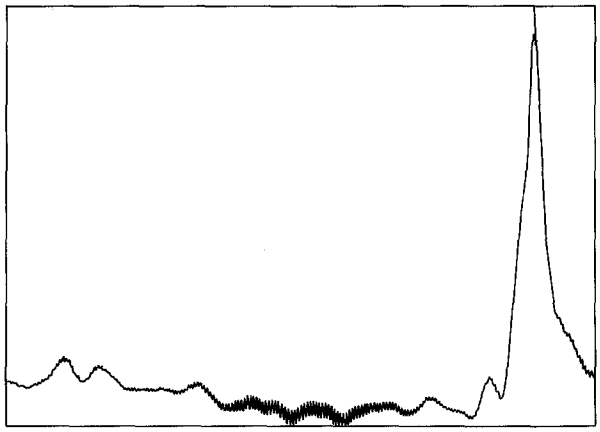

Figure 24 An experimental $V(z)$ curve obtained at 0° from the Pysic specimen.

TABLE VI A comparison of the mean Rayleigh wave velocity (v) and attenuation (α) as measured on the LFBM for pure and whisker-reinforced alumina specimens

	Vitox Al_2O_3	Argonne Al_2O_3	Al_2O_3/SiC A	Al_2O_3/SiC B
v (m sec^{-1})	5836.7	5837.5	5837.9	5843.6
α ($\times 10^{-1}$)	0.1105	0.1155	0.1492	0.1433

TABLE VII Comparison of calculated and experimental shear wave velocities for (m sec^{-1}) for whisker-reinforced alumina with pure alumina

	Al_2O_3/SiC	Al_2O_3
Calculated Voigt average	6565	6350
Calculated Reuss average	6550	6350
Argonne data (20 MHz)*	6482	6350
Oxford data (228 MHz)	6382†	6358§
	6370‡	6357¶

*Obtained by D. Kupperman, University of Chicago, USA.
† Area A, SiC whiskers more parallel.
‡ Area B, SiC whiskers less parallel.
§ Argonne alumina sample.
¶ Vitox alumina sample.

Laboratory) for supplying most of the specimens and for discussion of the results. Mr P. Lemaitre carried out the indentation tests of the ceramic specimens, and Dr D. Kupperman (Argonne National Laboratory, USA) provided silicon carbide-reinforced alumina and alumina specimens. This study was partly funded by the Underlying Programme of the UKAEA.

References

1. S. Y. SOKOLOV, USSR Patent no. 49 (1936).
2. F. DUNN and W. J. FRY, *J. Acoustic Soc. Amer.* **31** (1959) 632.
3. C. F. QUATE, A. ATALAR and H. K. WICKRAMASINGHE, *Proc. IEEE* **67** (1979) 1092.
4. R. A. LEMONS and C. F. QUATE, *Appl. Phys. Lett.* **25** (1974) 251.

Figure 25 A scanning electron micrograph of a fracture surface of the whiskers-reinforced alumina specimen. The silicon carbide whiskers are 10 μm × 0.7 μm in size (courtesy of D. Kupperman, Argonne National Laboratory).

5. V. JIPSON and C. F. QUATE, *ibid.* **32** (1978) 789.
6. B. HADIMIOGLU and J. S. FOSTER, *J. Appl. Phys.* **56** (1984) 1976.
7. M. HOPPE and A. ATALAR, *Rev. Sci. Instrum.* **57** (1986) 2568.
8. G. A. D. BRIGGS, "An introduction to scanning acoustic microscopy", Royal Microscopical Society Handbook 12 (Oxford University Press, 1985).
9. M. HOPPE and J. BEREITER-HAHN, *IEEE Trans. Sonics Ultrasonics* **SU-32** (1985) 289.
10. W. PARMON and H. L. BERTONI, *Electron. Lett.* **15** (1979) 684.
11. H. L. BERTONI, *IEEE* **SU-31** (1984) 105.
12. R. D. WEGLEIN, *Appl. Phys. Lett.* **34** (1979) 179.
13. A. ATALAR, *J. Appl. Phys.* **49** (1978) 5130.
14. J. KUSHIBIKI and N. CHUBACHI, *IEEE Trans. Sonics Ultrasonics* **SU-32** (1985) 189.
15. B. R. LAWN and T. R. WILSHAW, *J. Mater. Sci.* **10** (1975) 1049.
16. B. R. LAWN, A. G. EVANS and D. B. MARSHALL, *J. Amer. Ceram. Soc.* **63** (1980) 574.
17. K. YAMANAKA, J. KUSHIBIKI and N. CHUBACHI, *Electron. Lett.* **21** (1985) 165.
18. K. YAMANAKA, Y. ENOMOTO and Y. TSUYA, *IEEE Trans. Sonics Ultrasonics* **SU-32** (1985) 313.
19. S. K. DATTA, H. M. LEDBETTER, Y. SHINDO and A. H. SHAH, Interface effects on attenuation and phase velocities in metal-matrix composites, "Review of progress in quantitative nondestructive evaluation", Vol. 7, edited by D. O. Thompson and D. E. Chimenti (Plenum, New York, 1986).

Received 29 March
and accepted 26 April 1988